nature physics

ARTICLES

https://doi.org/10.1038/s41567-022-01704-x

Selective and collective actuation in active solids

P. Baconnier[1]✉, D. Shohat[1,2], C. Hernández López[3,4], C. Coulais[5], V. Démery[1,6], G. Düring[3,4] and O. Dauchot[1]✉

Active solids consist of elastically coupled out-of-equilibrium units performing work[1–13]. They are central to autonomous processes, such as locomotion, self-oscillations and rectification, in biological systems[14–25], designer materials[26] and robotics[27–31]. Yet, the feedback mechanism between elastic and active forces as well as the possible emergence of collective behaviours in a mechanically stable elastic solid remains elusive. Here we introduce a minimal realization of an active elastic solid in which we characterize the emergence of selective and collective actuation resulting from the interplay between activity and elasticity. Polar active agents exert forces on the nodes of a two-dimensional elastic lattice. The resulting displacement field nonlinearly reorients the active agents. For a large-enough coupling, a collective oscillation of the lattice nodes around their equilibrium position emerges. Only a few elastic modes are actuated and crucially, they are not necessarily the lowest energy ones. By combining experiments with the numerical and theoretical analyses of an agent's model, we unveil the bifurcation scenario and selection mechanism by which the collective actuation takes place. Our findings may provide a new mechanism for oscillatory dynamics in biological systems[14,19,21,24] and the opportunity for bona fide autonomy in metamaterials[32,33].

Active solids[1–13] combine the central properties of simple elastic solids and active liquids[34–39] (Fig. 1a). On one hand, the positional degrees of freedom of their constituting units have a well-defined reference state. On the other hand, activity endows these units with an additional free degree of freedom in the form of polar, or dipolar, active forces. In active liquids, aligning interactions between these forces lead to collective motion. In active solids, these active forces deform the elastic matrix and induce a strain field, which depends on the forces' configuration. This strain tensor will, in turn, reorient the forces. This generic nonlinear elasto-active feedback, a typical realization of which is the contact inhibition of locomotion of cells[14,19], opens the path towards spontaneous collective excitations of the solid, which we call collective actuation. In this work, we propose a minimal experimental setting and numerical model in which we unveil the modal selectivity of collective actuation and its underlying principles.

We consider crystalline lattices with an active particle (at the center of each node) with a fluctuating orientation (Fig. 1b and Methods). Each node has a well-defined reference position, but will be displaced by the active particles (Fig. 1c). In contrast, the polarization of each particle is free to rotate and reorients towards its displacement (Fig. 1d, Supplementary Section 2.2.2 and Supplementary Video 1). This nonlinear feedback between deformations and polarizations is characterized by two length scales: (1) the typical elastic deformation caused by active forces l_e (Fig. 1c) and (2) the self-alignment length l_a (Fig. 1d). We complement the experiments with numerical simulations of elastically coupled self-aligning active particles[40] (Methods). In the overdamped, harmonic and noiseless limits, the model reads

$$\dot{\mathbf{u}}_i = \pi\hat{\mathbf{n}}_i - \mathbb{M}_{ij}\mathbf{u}_j, \tag{1a}$$

$$\dot{\mathbf{n}}_i = (\hat{\mathbf{n}}_i \times \dot{\mathbf{u}}_i) \times \hat{\mathbf{n}}_i, \tag{1b}$$

where the ratio of the elasto-active and self-alignment lengths, $\pi = l_e/l_a$, which we refer to as the elasto-active feedback, is the unique control parameter. Here $\hat{\mathbf{n}}_i$ is the polarization unit vector, $\mathbf{u}_i$ is the displacement field with respect to the reference configuration and $\mathbb{M}$ is the dynamical matrix (Supplementary Section 3.1).

If not hold, such an active solid adopts the translational and/or rotational rigid-body motion dictated by the presence of zero modes (Supplementary Videos 2 and 3), as reported in other theoretical models[3,5,16]. Here we are interested in stable elastic solids, with no zero modes. We, therefore, explore the emergence of collective dynamics in elastic lattices pinned at their edges. For both triangular (Fig. 2, top) and kagome (Fig. 2, bottom) lattices, we observe a regime in which all the lattice nodes spontaneously break chiral symmetry and rotate around their equilibrium position in a collective steady state (Fig. 2a and Supplementary Videos 5 and 8). This dynamical and chiral phase, which is reminiscent of oscillations in biological tissues[15,24], is clearly different from collective dynamics in active fluids[35,36] and rigid-body motion in active solids[3,5,9].

The dynamics are best described when projected on the normal modes of the elastic structure sorted by order of growing energies. The dynamics mostly condensate on two modes (Fig. 2b) and describe a limit cycle driven by the misalignment of the polarity and displacements (Fig. 2d). In the case of the triangular lattice, the selected modes are the two lowest-energy ones. Interestingly, in the case of the kagome lattice, these are the fourth and fifth modes, not the lowest-energy ones. For both lattices, the selected pair of degenerated modes are strongly polarized along one spatial direction; they are extended and the polarization of modes in each pair are locally quasi-orthogonal (Fig. 2c). The numerical simulations confirm the experimental observations, indicating that collective actuation is already present in the harmonic approximation and is not of inertial origin. It also allows the observation of additional peaks in the spectrum, which belong to the same symmetry class as the two most actuated modes (Fig. 2b and Supplementary Section

[1]Gulliver UMR CNRS 7083, ESPCI Paris, Université PSL, Paris, France. [2]School of Physics and Astronomy, Tel Aviv University, Tel Aviv, Israel. [3]Instituto de Física, Pontificia Universidad Católica de Chile, Santiago, Chile. [4]ANID—Millenium Nucleus of Soft Smart Mechanical Metamaterials, Santiago, Chile. [5]Van der Waals-Zeeman Institute, Institute of Physics, Universiteit van Amsterdam, Amsterdam, The Netherlands. [6]Univ Lyon, ENSL, CNRS, Laboratoire de Physique, Lyon, France. ✉e-mail: paul.baconnier@espci.fr; olivier.dauchot@espci.fr

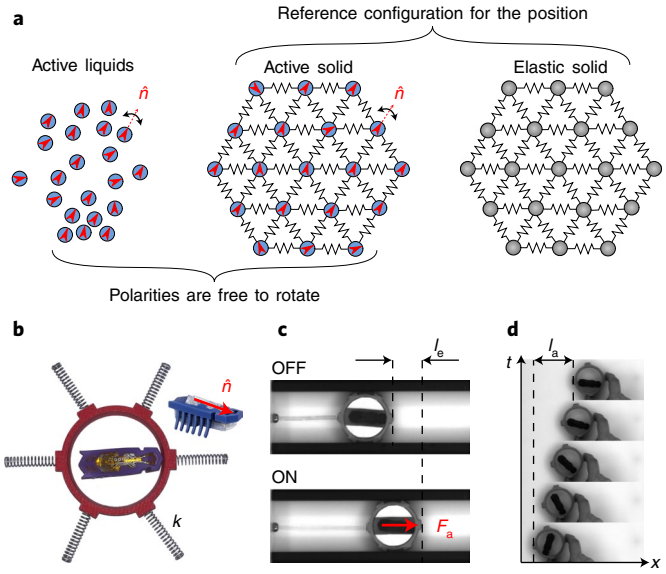

Fig. 1 | Active-solids design principle. a, Active solids have positional degrees of freedom with a reference state, and a free-to-rotate polarity vector in the direction of the active force. **b**, Active unit: a HEXBUG is trapped in a three-dimensionally printed cylinder. **c**, The active component, confined here in a linear track and attached to a spring of stiffness k, produces an active force of amplitude F_0 in the direction of polarity $\hat{\mathbf{n}}$ and elongates the spring by length $l_e = F_0/k$. **d**, Mechanical design of the HEXBUG—mass distribution and shape of the legs—is responsible for its alignement towards its displacement, here imposed manually, of the cylinder (Supplementary Information provides a quantitative measure of the self-alignment length l_a).

7). As evident below, these properties are at the root of the selection principle of the actuated modes.

The transition to the collective actuation regime (Fig. 2e) is controlled by the elasto-active feedback. The larger it is, the more the particles reorient on elastic deformations. Below the first threshold π_{FD}, the active solid freezes in a disordered state, with random polarizations and angular diffusion (Supplementary Videos 4 and 7). Beyond the second threshold π_{CA}, collective actuation sets in: synchronized oscillations take place and the noiseless dynamics follow a limit cycle, composed of several frequencies in a rational ratio (Supplementary Section 10.2). In between, the system is heterogeneous (Fig. 2f and Supplementary Video 6), with the oscillating dynamics being favoured close to the center, whereas the frozen disordered regime invades the system layer by layer, from the edges towards the center, as π decreases (Supplementary Video 11).

Simulations with increasing values of N, as the physical size L is kept constant (Methods), indicate that collective actuation subsists for large N (Fig. 3). The successive deactuation steps converge towards a regular variation of the fraction of nodes activated in the center of the system, f_{CA} (Fig. 3c,d and Supplementary Videos 12 and 13). At the transition to the frozen disordered state, when $\pi = \pi_{FD}$, the fraction of actuated nodes drops discontinuously to zero, from a finite value f^*_{CA}, which decreases with N, but saturates at large N (Fig. 3d). In the case of triangular lattices, the collective oscillation frequency Ω, measured in the region of collective actuation, continuously decreases to zero (Fig. 3d, top). This is, however, non-generic: in the case of kagome lattices, very close to the transition, the dynamics condensate on a different set of modes, pointing at the possible multiplicity of periodic solutions. The transition is essentially discontinuous. Most importantly, the spectrum demonstrates that inside the collective actuation regime, the symmetry class of modes that is selected is independent of the system size (Fig. 3e). The selection of the most actuated modes is again dictated by the geometry of the modes and not only by their energies. In all cases, the condensation level remains large, with a large condensation fraction $\lambda_{1/2}$ (Methods) for a wide range of values of π (Fig. 3d, inset).

Altogether, our experimental and numerical findings demonstrate the existence of a selective and collective actuation in active solids. This new kind of collective behaviour specifically takes place because of the elasto-active feedback, that is, the reorientation of the active units by the displacement field. The salient features of collective actuation are threefold: (1) transition from the disordered phase leads to a chiral phase with spontaneously broken symmetry; (2) actuated dynamics are not of inertial origin; they take place on a few modes and are not always the lowest-energy ones, and therefore, they obey non-trivial selection rules; (3) transition follows the coexistence scenario, where the fraction of actuated nodes discontinuously falls to zero. Hereafter, we unveil the physical origins of these three attributes.

At large scales, the dynamics of the displacement and polarization fields, $\mathbf{U}(\mathbf{r},t)$ and $\mathbf{m}(\mathbf{r},t)$—the local averages of microscopic displacements $\mathbf{u}_i$ and polarizations $\hat{\mathbf{n}}_i$, respectively—are obtained from a coarse-graining procedure (Supplementary Section 6) and are read as

$$\partial_t \mathbf{U} = \pi \mathbf{m} + \mathbf{F}_e, \tag{2a}$$

$$\partial_t \mathbf{m} = (\mathbf{m} \times \partial_t \mathbf{U}) \times \mathbf{m} + \frac{1 - \mathbf{m}^2}{2} \partial_t \mathbf{U} - D_r \mathbf{m}, \tag{2b}$$

where the elastic force $\mathbf{F}_e[\mathbf{U}]$ is given by the choice of a constitutive relation and the relaxation term $-D_r\mathbf{m}$ results from the noise. Assuming linear elasticity, the frozen phase, in which the local random polarities and displacements average to $\mathbf{U}=\mathbf{0}$ and $\mathbf{m}=\mathbf{0}$, is stable for small elasto-active feedback. It becomes linearly unstable for $\pi > \pi_c^{cg} = 2\,\omega^2_{min}$, where ω^2_{min} is the smallest eigenvalue of the linear elastic operator (Supplementary Section 6.5). We then look for homogeneous solutions, assuming condensation on two degenerated and spatially homogeneous modes, such that $\mathbf{F}_e = -\omega_0^2\mathbf{U}$, where ω_0^2 is the eigenfrequency of such modes. For $\pi > \omega_0^2$, we find a polarized chiral phase oscillating at frequency

$$\Omega = \omega_0 \sqrt{\pi - \omega_0^2}. \tag{3}$$

In the limiting case $D_r = 0$, $|m| = 1$ (Supplementary Section 6.6). The resulting mean-field phase diagram (Fig. 4a), thus, captures the existence of frozen and chiral phases and their phase-space coexistence for a finite range of elasto-active feedback. However, with the disordered $\mathbf{m}=\mathbf{0}$ and the polarized chiral oscillating solutions being disconnected, the nature of the transition is controlled by inhomogeneous solutions, which cannot be investigated within perturbative approaches.

Alternatively, we turn ourselves to simpler geometries in which exact results can be obtained. The first important hint at the nature of the transition towards the chiral phase concerns the structure of the phase space and is best understood by considering the dynamics of a single particle (Fig. 4b, Supplementary Videos 9 and 10 and Supplementary Section 5). Below $\pi_c = \omega_0^2$, the phase space for displacements contains an infinite set of marginal fixed points, organized along a circle of radius $R = \pi/\omega_0^2$. At π_c, the escape rate of polarity—away from its frozen orientation—becomes faster than the restoring dynamics of displacement. As a result, the later permanently chases the polarity and stable rotation sets in. All the fixed points become unstable at once; and a limit cycle of radius

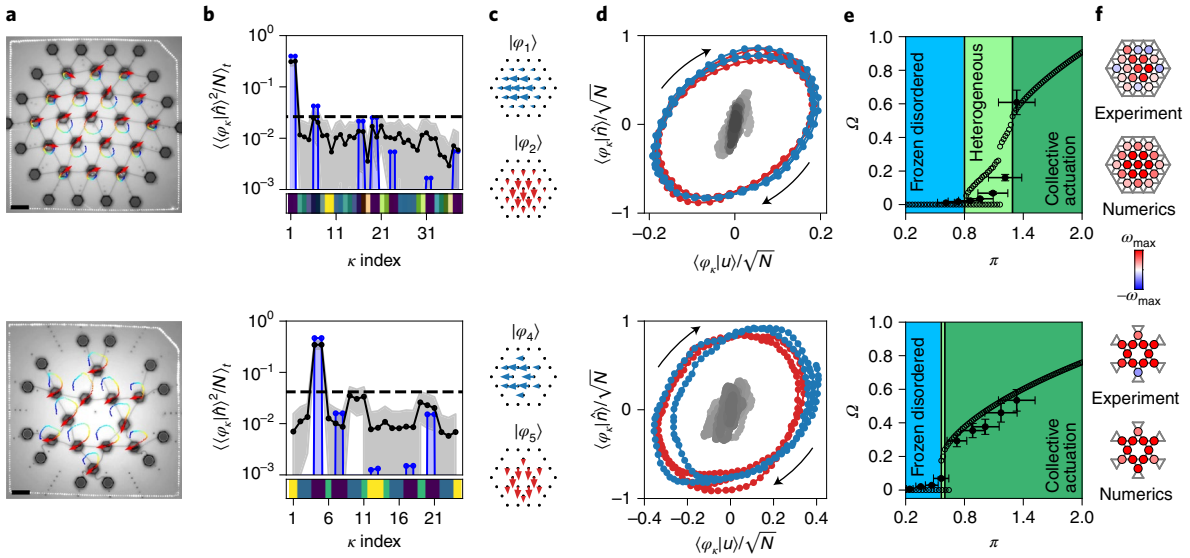

Fig. 2 | Selective and collective actuation in two-dimensional elastic lattices, pinned at their edges. The panels in the top row refer to a triangular lattice with $N=19$; those in the bottom row refer to a kagome lattice with $N=12$. **a**, When embedded in an elastic lattice, a large-enough elasto-active feedback π drives the system towards collective actuation dynamics (red arrows, polarities $\hat{\mathbf{n}}_i$; trajectories are colour coded from blue to red with respect to increasing time; scale bars, 10 cm). **b**, Spectral decomposition of the dynamics on the normal modes of the lattices, sorted by order of growing energies (grey, experiments; blue, numerics). The horizontal dashed lines indicate equipartition. The bottom colour bars code for the symmetry class of the modes (Supplementary Section 7). The grey area represents the 1σ confidence interval on the experimental measurement. **c**, Schematic of the two most excited modes, which are not necessarily the lowest-energy ones. **d**, Normal-mode components of the active forces as a function of the normal-mode components of the displacements (blue/red, projection on the data in **c**; grey, other modes). The symbol size is set to represent the 1σ confidence interval on the experimental measurement. **e**, Transition to the collective actuation regime: average oscillation frequency Ω as a function of π (plain bullets, experiments; open circles, numerics). Background colours code for the dynamical regime (light blue, frozen and disordered; light green, heterogeneous (H); dark green, collective actuation). Triangular: $\pi_{FD}=0.800$, $\pi_{CA}=1.290$; kagome: $\pi_{FD}=0.564$, $\pi_{CA}=0.600$. The error bars represent the 1σ confidence intervals, inherited from the uncertainty in the microscopic parameter measurements. **f**, Individual oscillation frequencies ω_i illustrating the coexistence dynamics in experiments and numerical simulations (triangular lattice, $\pi_{exp}/\pi_{num}=1.220/1.090$; kagome lattice, $\pi_{exp}/\pi_{num}=0.723/0.564$).

$R=\left(\pi/\omega_0^2\right)^{1/2}$ and oscillation frequency $\Omega=\omega_0\sqrt{\pi-\omega_0^2}$, identical to the one obtained from the mean-field approach, continuously branches off (Fig. 4c,d). Note that the oscillating dynamics does not arise from a Hopf bifurcation, but from the global bifurcation of a continuous set of fixed points into a limit circle.

Understanding how the nonlinear coupling of N such elementary units leads to the selection mechanism of the actuated modes requires a more involved analysis. From equation (1), it is evident that any configuration $\left(\{\hat{\mathbf{n}}_i\},\left\{\mathbf{u}_i=\pi\mathbb{M}_{ij}^{-1}\hat{\mathbf{n}}_j\right\}\right)$ is a fixed point of the dynamics. In contrast with the one-particle case, the linear destabilization threshold $\pi_c(\{\hat{\mathbf{n}}_i\})$ depends on the fixed-point configuration (Supplementary Section 4.4). These thresholds are bounded: $\pi_c^{\min}\leq\pi_c(\{\hat{\mathbf{n}}_i\})\leq\pi_c^{\max}$. A first fixed point becomes unstable for $\pi=\pi_c^{\min}=\omega_{\min}^2$, where $\omega_{\min}^2$ is the smallest eigenvalue of the dynamical matrix $\mathbb{M}$ (Supplementary Section 4.5) and an upper bound for $\pi_c^{\max}$ (Supplementary Section 4.6) reads

$$\pi^{\text{upp}}=\min_{\{i,j\}}\left(\frac{\omega_i^2+\omega_j^2}{c\left(|\boldsymbol{\varphi}_i\rangle,|\boldsymbol{\varphi}_j\rangle\right)}\right). \tag{4}$$

The function $c(\bullet,\bullet)$ only depends on the eigenvectors of $\mathbb{M}$, namely, $\{|\varphi_i\rangle\}$. It is bounded between 0 and 1 and is the maximum when modes $|\varphi_i\rangle$ and $|\varphi_j\rangle$ are extended and locally orthogonal. More specifically, the pair of modes that dominates the dynamics, that is, $\{|\varphi_1\rangle,|\varphi_2\rangle\}$ for the triangular lattice and $\{|\varphi_4\rangle,|\varphi_5\rangle\}$ for the kagome lattice, are precisely the ones that optimize the bound. The construction of this bound is very general. It demonstrates that for any stable elastic structure, there is a strength of the elasto-active feedback above which the frozen dynamics is unstable and a dynamical regime must set in. It also captures the mode selection in the strongly condensed regime. Our findings about the linear stability of the fixed points for the triangular and kagome lattices are summarized in Extended Data Fig. 1.

The fact that some fixed points loose stability does not imply that collective actuation sets in: from these fixed points, the system can either slide into a neighbouring stable fixed point or condensate on some dynamical attractor. An exact theory to describe this condensation process is still missing in the general case, but can be formulated in the simpler, yet rich-enough, case of a linear chain of N active particles, fixed at both ends. In the zero-rest length limit of the springs, the rotational invariance of the dynamical equations ensures that the eigenvalues and eigenvectors of the dynamical matrix are degenerated by pairs of locally orthogonal modes. In such a situation, the limit-cycle solution, corresponding to the collective actuation regime, is analytically found (Supplementary Section 9.2), leading to a precise transition diagram (illustrated here for $N=7$; Fig. 4e). When π exceeds the threshold value π_{CA}, the limit cycle is stable. We have checked that it is the only stable periodic solution, up to $N=20$. If $\pi_{CA}\leq\pi\leq\pi_c^{\max}$, it coexists with an infinite number of stable fixed points. The evolution of their respective basins of attraction can be largely understood by studying the $N=2$ case (Supplementary Section 9.3.1 and Supplementary Fig. 9). For $\pi<\pi_{CA}$, the dynamics leave the limit cycle and become heterogeneous.

The physical origin of spatial coexistence lies in the normalization constraint of the polarity field, namely, $\|\hat{\mathbf{n}}_i\|=1$, which translates into a strong constraint over the radii of rotation, namely,

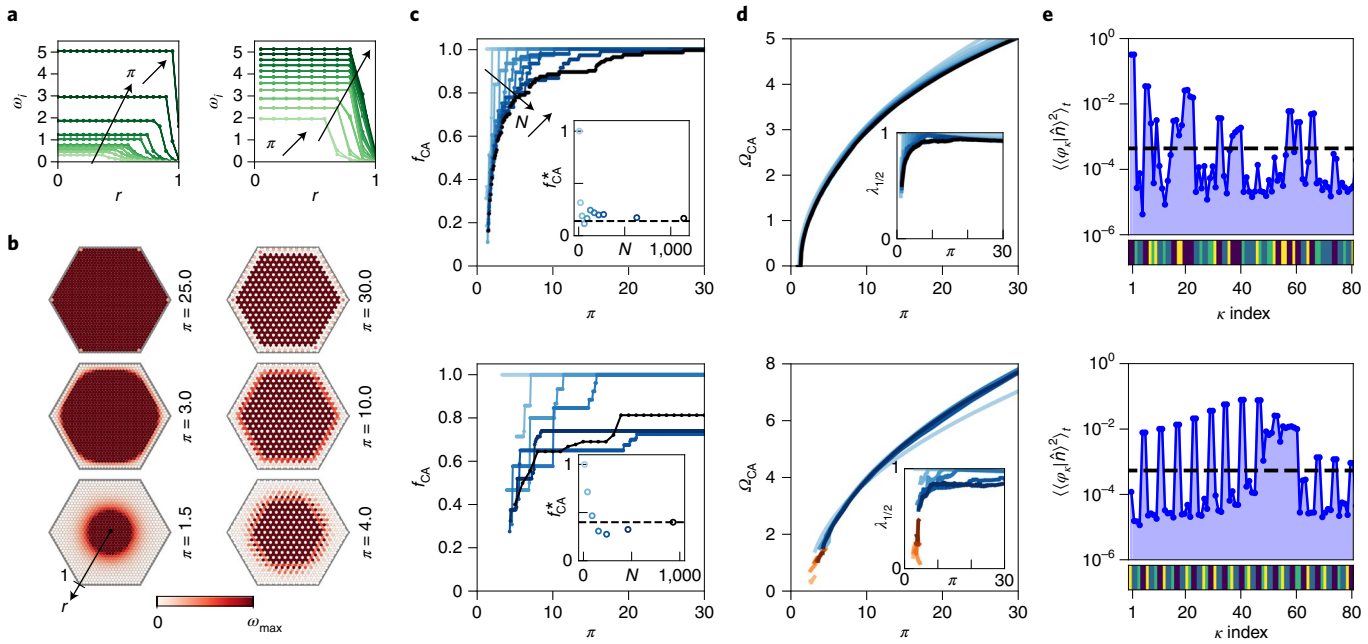

Fig. 3 | Large-*N* lattices. a, Radial distribution of the individual oscillation frequencies ω_i (left, triangular lattice with $N=1{,}141$; right, kagome lattice with $N=930$). The plots are colour coded from light to dark green as π increases (triangular lattice, for $\pi \in [1.5, 1.6, 1.7, 1.8, 1.9, 2.0, 2.5, 3.0, 5.0, 10.0, 30.0]$; kagome lattice, for $\pi \in [4.0, 5.0, 6.0, 7.0, 8.0, 9.0, 10.0, 11.0, 12.0, 13.0, 14.0]$). **b**, Spatial distribution of $|\omega_i|$ (left, triangular lattice with $N=1{,}141$; right, kagome lattice with $N=930$); the π values are as indicated. **c**, Collective actuation fraction f_{CA} as a function of π for increasing N, colour coded from light to dark blue (the inset shows that f_{CA} at the onset of collective actuation saturates to a finite value at large N). **d**, Collective oscillation frequency Ω_{CA} as a function of π for increasing N; the same colour code is followed (triangular lattices, $N=7, 19, 37, 61, 91, 127, 169, 217, 271, 631, 1{,}141$; kagome lattice, $N=12, 42, 90, 156, 240, 462, 930$) (the inset shows the condensation fraction on the selected symmetry class, $\lambda_{1/2}$, as a function of π for increasing N). **e**, Spectral decomposition of the dynamics on the normal modes of the lattices, sorted by order of growing energies (only the first 80 modes are shown, both for $\pi=10$). For **c**–**e**, the top row shows the data for the triangular lattice and the bottom row, for the kagome lattice.

$R_i \geq 1$ (Supplementary Sections 9.2.3 and 9.2.4). Whenever R_i becomes unity, the polarity and displacement vectors become parallel, freezing the dynamics. The spatial distribution of R_i is set by that of the modes selected by collective actuation, with particles closer to the boundaries having typically a smaller radius of rotation than the ones at the center. The threshold value π_{CA}, below which the dynamics leave the limit cycle, is precisely met when the particles at the boundary reach a radius of rotation $R=1$. For $\pi < \pi_{CA}$, competition between the outer particles (which want to freeze) and the central particles (which want to cycle) leads to the sequential layer-by-layer deactuation (Fig. 4f) for a linear chain with $N=7$ and observed both experimentally and numerically. The threshold value π_{FD} is reached when, eventually, the remaining particles at the center freeze and the system discontinuously falls into the frozen disordered state.

Altogether, we have shown that (1) the chiral phase takes its origin in the one-particle dynamics; (2) the selection of modes results from the nonlinear elasto-active feedback, which connects the linear destabilization of the fixed points to the spatial extension and local orthogonality of pairs of modes; (3) spatial coexistence emerges from the normalization constraint of the polarity fields.

The role of noise, which was not considered in numerical and theoretical analysis, is another matter of interest. In the frozen disordered regime, noise is responsible for the angular diffusion of polarities amongst the fixed points. In the collective actuation regime, the noise level present in the experiment does not substantially alter the dynamics. Numerical simulations confirm that there is a sharp transition at a finite noise amplitude D_c, below which collective actuation is sustained (Extended Data Fig. 2a). For noise amplitude much lower than D_c, the noise merely reduces the mean angular frequency Ω (Extended Data Fig. 2b). Closer to the transition, the noise allows for stochastic inversions of the direction of rotation, restoring the chiral symmetry (Extended Data Fig. 2c).

Finally, it has been shown very recently that non-symmetrical interactions, together with non-conservative dynamics, generically lead to chiral phases[41]. Here the polarity and displacement vectors of a single particle do experience non-symmetrical interactions, the phase of the displacement chasing that of the polarity. By mapping the coarse-grained equations to the most general equations, one can write for rotationally symmetric vectorial order parameters[41]; we find that the macroscopic displacement and polarity fields also couple non-symmetrically (Methods). This suggests a possible description of the transition to collective actuation in terms of non-reciprocal phase transitions. If this were to be confirmed by a more involved analysis of the large-scale dynamics, it would motivate the study of disordered-to-chiral phase transition in active solids, which has not been addressed theoretically yet. In the same vein, one may ask whether the coarse-grained system shall obey standard or odd elasticity[13].

More generally, the recent miniaturization of autonomous active units[42] opens the path towards the extension of our design principle to the scale of materials science. In this context, extending the relation between the structural design of active materials—including the geometry and topology of the lattice, presence of disorder and inclusion of doping agents—and their spontaneous actuation offers a wide range of perspectives.

Online content

Any methods, additional references, Nature Research reporting summaries, source data, extended data, supplementary information,

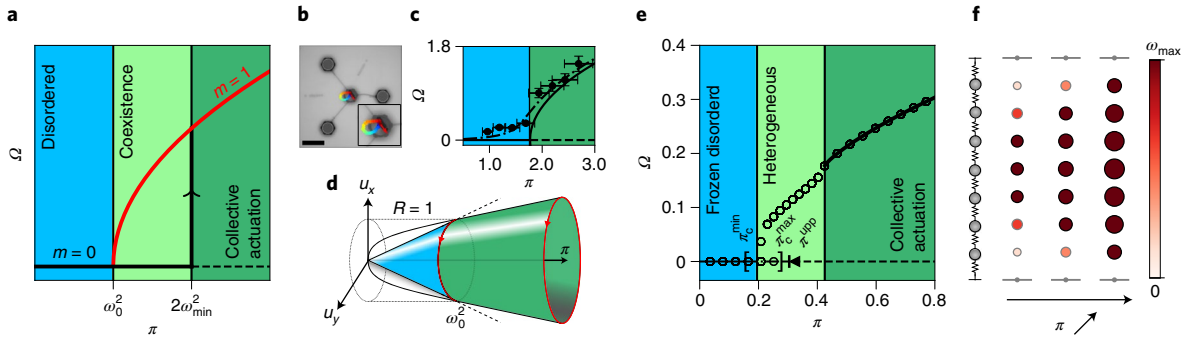

Fig. 4 | Mean-field, single-particle, one-dimensional-lattice phase diagrams. a, At the mean-field level, the disordered $\mathbf{m}=0$ phase (black line) coexists with the fully polarized ($|\mathbf{m}|=1$) chiral ($\Omega>0$) phase (red line) for $\pi \in \left[\omega_0^2, 2\omega_{\mathrm{min}}^2\right]$. **b**,**c**, A single active unit connected to three static vertices of a regular triangle (red arrow, polarity $\hat{\mathbf{n}}$; trajectories are colour coded from blue to red with respect to increasing time; scale bar, 10 cm; the inset shows a zoomed-in view of the active unit) (**b**) and it oscillates with an average rotation frequency Ω increasing with π (**c**); (•, experimental data; continuous line, analytical expression (equation (3)); dot-dash line, numerical values in the presence of a bias; $\pi_c=1.77$). The error bars represent the 1σ confidence intervals, inherited from the uncertainty in the microscopic parameter measurements. **d**, Phase-space structure of the displacements: for $\pi < \omega_0^2$, an infinite set of marginal fixed points forms a circle of radius $R = \pi/\omega_0^2$; for $\pi > \omega_0^2$, all such fixed points are unstable and a limit cycle of radius $R = \left(\pi/\omega_0^2\right)^{1/2}$ branches off continuously. **e**,**f**, Collective actuation in a zero-rest chain length of $N=7$ nodes, pinned at both ends. **e**, Average oscillation frequency Ω as a function of π (continuous line, limit cycle found analytically; horizontal lines ($\Omega=0$), range of existence of only stable (continuous), only unstable (dashed) and coexisting stable and unstable (dot-dash) fixed points; ∘, numerical data; the same background colour as that in Fig. 2e). $\pi_c^{\mathrm{min}}=0.152$, $\pi_c^{\mathrm{max}}=0.280$, $\pi_c^{\mathrm{upp}}=0.304$, $\pi_{\mathrm{FD}}=0.195$, $\pi_{\mathrm{CA}}=0.426$. **f**, Individual oscillation frequencies ω_i for increasing values of $\pi=[0.20, 0.33, 1.00]$ in the $N=7$ chain. The radii of the coloured circles code for the average trajectory radius. The black and grey contours indicate $R_i \geq 1$ and $R_i \leq 1$, respectively.

acknowledgements, peer review information; details of author contributions and competing interests; and statements of data and code availability are available at https://doi.org/10.1038/s41567-022-01704-x.

Received: 21 September 2021; Accepted: 30 June 2022;
Published online: 18 August 2022

References

1. Koenderink, G. H. et al. An active biopolymer network controlled by molecular motors. *Proc. Natl Acad. Sci. USA* **106**, 15192–15197 (2009).
2. Henkes, S., Fily, Y. & Marchetti, M. C. Active jamming: self-propelled soft particles at high density. *Phys. Rev. E* **84**, 040301 (2011).
3. Menzel, A. M. & Löwen, H. Traveling and resting crystals in active systems. *Phys. Rev. Lett.* **110**, 055702 (2013).
4. Berthier, L. & Kurchan, J. Non-equilibrium glass transitions in driven and active matter. *Nat. Phys.* **9**, 310–314 (2013).
5. Ferrante, E., Turgut, A. E., Dorigo, M. & Huepe, C. Elasticity-based mechanism for the collective motion of self-propelled particles with springlike interactions: a model system for natural and artificial swarms. *Phys. Rev. Lett.* **111**, 268302 (2013).
6. Prost, J., Jülicher, F. & Joanny, J.-F. Active gel physics. *Nat. Phys.* **11**, 111–117 (2015).
7. Ronceray, P., Broedersz, C. P. & Lenz, M. Fiber networks amplify active stress. *Proc. Natl Acad. Sci. USA* **113**, 2827–2832 (2016).
8. Woodhouse, F. G., Ronellenfitsch, H. & Dunkel, J. Autonomous actuation of zero modes in mechanical networks far from equilibrium. *Phys. Rev. Lett.* **121**, 178001 (2018).
9. Briand, G., Schindler, M. & Dauchot, O. Spontaneously flowing crystal of self-propelled particles. *Phys. Rev. Lett.* **120**, 208001 (2018).
10. Giavazzi, F. et al. Flocking transitions in confluent tissues. *Soft Matter* **14**, 3471–3477 (2018).
11. Klongvessa, N., Ginot, F., Ybert, C., Cottin-Bizonne, C. & Leocmach, M. Active glass: ergodicity breaking dramatically affects response to self-propulsion. *Phys. Rev. Lett.* **123**, 248004 (2019).
12. Maitra, A. & Ramaswamy, S. Oriented active solids. *Phys. Rev. Lett.* **123**, 238001 (2019).
13. Scheibner, C. et al. Odd elasticity. *Nat. Phys.* **16**, 475–480 (2020).
14. Abercrombie, M. & Heaysman, J. E. Observations on the social behaviour of cells in tissue culture: II. 'Monolayering' of fibroblasts. *Exp. Cell Res.* **6**, 293–306 (1954).
15. Vilfan, A. & Frey, E. Oscillations in molecular motor assemblies. *J. Phys.: Condens. Matter* **17**, S3901 (2005).
16. Szabo, B. et al. Phase transition in the collective migration of tissue cells: experiment and model. *Phys. Rev. E* **74**, 061908 (2006).
17. Mizuno, D., Tardin, C., Schmidt, C. F. & MacKintosh, F. C. Nonequilibrium mechanics of active cytoskeletal networks. *Science* **315**, 370–373 (2007).
18. Banerjee, S., Utuje, K. J. & Marchetti, M. C. Propagating stress waves during epithelial expansion. *Phys. Rev. Lett.* **114**, 228101 (2015).
19. Smeets, B. et al. Emergent structures and dynamics of cell colonies by contact inhibition of locomotion. *Proc. Natl Acad. Sci. USA* **113**, 14621–14626 (2016).
20. Bi, D., Yang, X., Marchetti, M. C. & Manning, M. L. Motility-driven glass and jamming transitions in biological tissues. *Phys. Rev. X* **6**, 021011 (2016).
21. Chen, C., Liu, S., Shi, X.-q, Chaté, H. & Wu, Y. Weak synchronization and large-scale collective oscillation in dense bacterial suspensions. *Nature* **542**, 210–214 (2017).
22. Needleman, D. & Dogic, Z. Active matter at the interface between materials science and cell biology. *Nat. Rev. Mater.* **2**, 17048 (2017).
23. Holmes, D. F. et al. Synchronized mechanical oscillations at the cell–matrix interface in the formation of tensile tissue. *Proc. Natl Acad. Sci. USA* **115**, E9288–E9297 (2018).
24. Peyret, G. et al. Sustained oscillations of epithelial cell sheets. *Biophys. J.* **117**, 464–478 (2019).
25. Henkes, S., Kostanjevec, K., Collinson, J. M., Sknepnek, R. & Bertin, E. Dense active matter model of motion patterns in confluent cell monolayers. *Nat. Commun.* **11**, 1405 (2020).
26. Brandenbourger, M., Locsin, X., Lerner, E. & Coulais, C. Non-reciprocal robotic metamaterials. *Nat. Commun.* **10**, 4608 (2019).
27. Brambilla, M., Ferrante, E., Birattari, M. & Dorigo, M. Swarm robotics: a review from the swarm engineering perspective. *Swarm Intell.* **7**, 1–41 (2013).
28. Pratissoli, F., Reina, A., Lopes, Y. K., Sabattini, L. & Groß, R. A soft-bodied modular reconfigurable robotic system composed of interconnected kilobots. In *2019 International Symposium on Multi-Robot and Multi-Agent Systems (MRS)* 50–52 (IEEE, 2019).
29. Li, S. et al. Particle robotics based on statistical mechanics of loosely coupled components. *Nature* **567**, 361–365 (2019).
30. Dorigo, M., Theraulaz, G. & Trianni, V. Reflections on the future of swarm robotics. *Sci. Robot.* **5**, eabe4385 (2020).
31. Oliveri, G., van Laake, L. C., Carissimo, C., Miette, C. & Overvelde, J. T. Continuous learning of emergent behavior in robotic matter. *Proc. Natl Acad. Sci. USA* **118**, e2017015118 (2021).
32. Bertoldi, K., Vitelli, V., Christensen, J. & Van Hecke, M. Flexible mechanical metamaterials. *Nat. Rev. Mater.* **2**, 17066 (2017).
33. Pishvar, M. & Harne, R. L. Foundations for soft, smart matter by active mechanical metamaterials. *Adv. Sci.* **7**, 2001384 (2020).
34. Toner, J. & Tu, Y. Long-range order in a two-dimensional dynamical XY model: how birds fly together. *Phys. Rev. Lett.* **75**, 4326–4329 (1995).

35. Vicsek, T. & Zafeiris, A. Collective motion. *Phys. Rep.* **517**, 71–140 (2012).
36. Bricard, A., Caussin, J.-B., Desreumaux, N., Dauchot, O. & Bartolo, D. Emergence of macroscopic directed motion in populations of motile colloids. *Nature* **503**, 95–98 (2013).
37. Marchetti, M. C. et al. Hydrodynamics of soft active matter. *Rev. Mod. Phys.* **85**, 1143 (2013).
38. Wittkowski, R. et al. Scalar φ^4 field theory for active-particle phase separation. *Nat. Commun.* **5**, 4351 (2014).
39. Peshkov, A., Bertin, E., Ginelli, F. & Chaté, H. Boltzmann-Ginzburg-Landau approach for continuous descriptions of generic Vicsek-like models. *Eur. Phys. J. Spec. Top.* **223**, 1315–1344 (2014).
40. Dauchot, O. & Démery, V. Dynamics of a self-propelled particle in a harmonic trap. *Phys. Rev. Lett.* **122**, 068002 (2019).
41. Fruchart, M., Hanai, R., Littlewood, P. B. & Vitelli, V. Non-reciprocal phase transitions. *Nature* **592**, 363–369 (2021).
42. Miskin, M. Z. et al. Electronically integrated, mass-manufactured, microscopic robots. *Nature* **584**, 557–561 (2020).

Acknowledgements

P.B. was supported by a PhD grant from ED564 'Physique en Ile de France'. D.S. was supported by a Chateaubriand fellowship. G.D. acknowledges support from Fondecyt grant no. 1210656 and ANID–Millenium Science Initiative Program—Code NCN17_092. We are grateful to M. Fruchart and V. Vitelli for fruitful discussions regarding non-reciprocity in elastic materials.

Author contributions

O.D., C.C. and G.D. conceived the project. P.B. and D.S. performed the experiments. P.B., D.S. and O.D. analysed the experimental results. P.B., V.D., O.D., C.H.L. and G.D. worked out the theory. All the authors contributed to the writing of the manuscript.

Competing interests

The authors declare no competing interests.

Additional information

Extended data is available for this paper at https://doi.org/10.1038/s41567-022-01704-x.

Supplementary information The online version contains supplementary material available at https://doi.org/10.1038/s41567-022-01704-x.

Correspondence and requests for materials should be addressed to P. Baconnier or O. Dauchot.

Peer review information *Nature Physics* thanks Anton Souslov and the other, anonymous, reviewer(s) for their contribution to the peer review of this work.

Reprints and permissions information is available at www.nature.com/reprints.

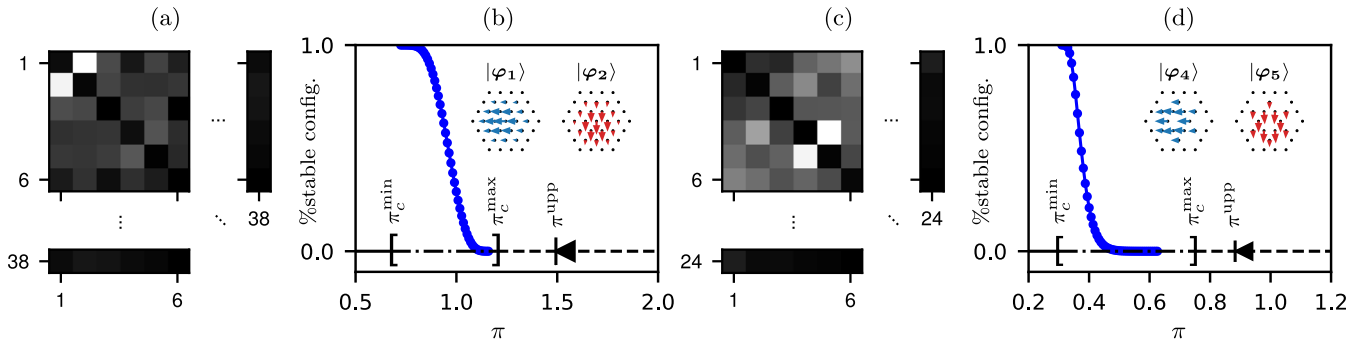

Extended Data Fig. 1 | Fixed points stability thresholds for the experimental's structures. (a/c) Stability thresholds upper-bound $\pi_{c,u}^{\{j,k\}}$ computed from Eq. (S45) for every pair of modes. The darker the pixel, the greater the upper-bound found. Remarkably, the best bound is always achieved for the pair of modes concerned by the condensation. (b/d) Fraction of stable fixed points as a function of π. The fraction of stable fixed points (•) is computed by integrating the histogram of the stability thresholds found by Eq. (S36) on one million configurations of the polarity field, drawn randomly and independently. Inset: sketch of the two most excited modes, which realized the best bound in (a/c). (a/b) For the triangular lattice pinned at the edges (α=1.29). $\pi_c^{\min} = 0.676$, $\pi_c^{\max} = 1.20$, $\pi_c^{\text{upp}} = 1.49$ (c/d) For the kagome lattice pinned at the edges (α=1.02). $\pi_c^{\min} = 0.375$, $\pi_c^{\max} = 0.751$, $\pi_c^{\text{upp}} = 0.883$.

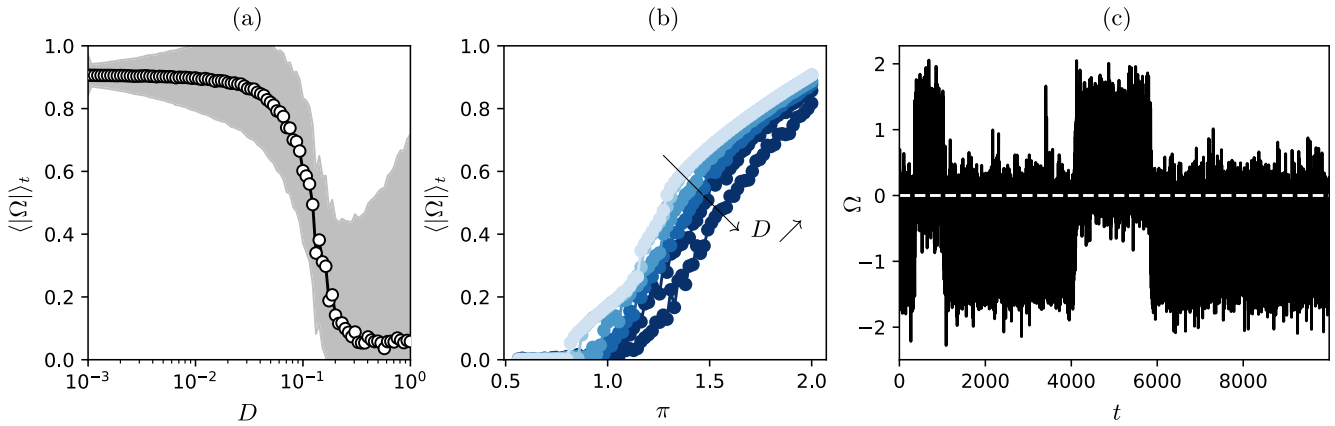

Extended Data Fig. 2 | Effect of the noise on the collective actuation regime. (a) Averaged (over time) mean angular frequency (over particles) in absolute value as a function of D for $\pi = 2.0$. The gray area represents the 1-σ fluctuations. (b) Averaged (over time) mean angular frequency (over particles) in absolute value as a function of π for increasing angular noise. From top to bottom, $D = 0, 10^{-3}, 10^{-2}, 2.10^{-2}, 5.10^{-2}$. Fluctuations are not shown for sake of clarity. (c) Mean (over particles) angular frequency as a function of time for $\pi = 2.0$ and $D = 10^{-1}$ in the triangular lattice pinned at the edges.